

UC Berkeley

UC Berkeley Previously Published Works

Title

Non-enzymatic glycation increases the failure risk of annulus fibrosus by predisposing the extrafibrillar matrix to greater stresses

Permalink

<https://escholarship.org/uc/item/4q44272f>

Authors

Zhou, Minhao
Archibeck, Erin S
Feteih, Yarah
[et al.](#)

Publication Date

2023-07-01

DOI

10.1016/j.actbio.2023.07.003

Copyright Information

This work is made available under the terms of a Creative Commons Attribution License, available at <https://creativecommons.org/licenses/by/4.0/>

Peer reviewed

1 **Non-enzymatic glycation increases the failure risk of annulus fibrosus by**
2 **predisposing the extrafibrillar matrix to greater stresses**
3
4

5 Minhao Zhou^{1, *}

6 Erin S. Archibeck^{1, *}

7 Yarah Feteih¹

8 Yousuf Abubakr¹

9 Grace D. O'Connell^{1,2}

10
11 ¹Department of Mechanical Engineering

12 University of California, Berkeley, USA

13 ²Department of Orthopaedic Surgery

14 University of California, San Francisco, USA

15
16 *: These authors contributed equally to this work
17
18

19 Submitted to: Acta Biomaterialia

20 Corresponding Author: Grace D. O'Connell

21 5122 Etcheverry Hall, #1740,

22 Berkeley, CA, 94720-1740

23 Phone: 510-642-3739

24 Fax: 510-643-5539

25 e-mail: g.oconnell@berkeley.edu

26 **Abstract**

27 Growing clinical evidence suggests a correlation between diabetes and more frequent and severe
28 intervertebral disc failure, partially attributed to accelerated advanced glycation end-products
29 (AGE) accumulation in the annulus fibrosus (AF) through non-enzymatic glycation. However, in
30 vitro glycation (i.e., crosslinking) reportedly improved AF uniaxial tensile mechanical properties,
31 contradicting clinical observations. Thus, this study used a combined experimental-computational
32 approach to evaluate the effect of AGEs on anisotropic AF tensile mechanics, applying the finite
33 element models (FEM) to complement experimental testing and examine difficult-to-measure
34 subtissue-level mechanics. Methylglyoxal-based treatments were applied to induce three
35 physiologically relevant AGE levels in vitro. Models incorporated crosslinks by adapting our
36 previously validated structure-based FEM framework. Experimental results showed that a
37 threefold increase in AGE content resulted in a ~55% increase in AF circumferential-radial tensile
38 modulus and failure stress and a 40% increase in radial failure stress. Failure strain was unaffected
39 by non-enzymatic glycation. Adapted FEMs accurately predicted experimental AF mechanics with
40 glycation. Model predictions showed that glycation increased stresses in the extrafibrillar matrix
41 under physiologic deformations, which may increase tissue mechanical failure or trigger catabolic
42 remodeling, providing insight into the relationship between AGE accumulation and increased
43 tissue failure. Our findings also added to the existing literature regarding crosslinking structures,
44 indicating that AGEs had a greater effect along the fiber direction, while interlamellar radial
45 crosslinks were improbable in the AF. In summary, the combined approach presented a powerful
46 tool for examining multiscale structure-function relationships with disease progression in fiber-
47 reinforced soft tissues, which is essential for developing effective therapeutic measures.

- 48 **Keywords:** Intervertebral disc; Annulus fibrosus; Advanced glycation end-products; Diabetes;
- 49 Tissue failure

50 **1. Introduction**

51 Low back pain is a prevalent global health concern affecting 80% of the adult population
52 and is the leading cause of productivity loss, disability, and healthcare expenditures in many
53 regions around the world [1]. The need for improved low back pain management has amplified in
54 recent years, driven by an aging population and the global diabetes epidemic [2-4]. Over the last
55 few decades, there has been a continual increase in global diabetes prevalence, with more than 10%
56 of the world's population being affected [3, 4]. Growing clinical evidence has linked diabetes to
57 intervertebral disc degenerative disorders. Particularly, diabetic patients are ~50% more likely to
58 be diagnosed with disc degenerative disorders, with a longer duration or poorer control of diabetes
59 correlating with a more severe level of degeneration [5-8]. Diabetes is also a significant risk factor
60 for lumbar disc herniation, reportedly increasing its risk by ~50% after correcting for other risk
61 factors such as age, body mass index, lifestyle, and disease history [9].

62 The intervertebral disc, situated between adjacent vertebrae in the spinal column, is a
63 fibrocartilaginous joint that plays a crucial biomechanical role during daily activities, including
64 supporting multiaxial spinal loads and motions, as well as dissipating energy. The disc is a highly
65 complex, heterogeneous, hierarchical structure comprising a soft gel-like nucleus pulposus center
66 surrounded by a tough, fiber-reinforced annulus fibrosus (AF) ring [10]. Particularly, the AF
67 consists of 15-25 concentric lamellae of angle-ply collagen fibers embedded in a hydrated
68 proteoglycan-rich extracellular matrix, resulting in excellent load-bearing and energy absorption
69 capacities [10]. However, the disc is highly avascular with limited self-healing capabilities; thus,
70 the heavy biomechanical demand placed on the disc makes the AF highly susceptible to catabolic
71 tissue remodeling with degeneration and disease [11, 12]. Such catabolic remodeling has been

72 shown to initiate, aggravate, or predispose the AF and surrounding structures to irreversible
73 mechanical damage (e.g., tears and disruption), causing debilitating low back pain [11, 12].

74 A well-documented diabetes-induced structural remodeling in the AF is the accelerated
75 formation and accumulation of advanced glycation end-products (AGE) via non-enzymatic
76 glycation [13-15]. AGEs are a heterogeneous group of chemical compounds that can form
77 irreversible crosslinks with extracellular proteins [13, 15]. The highly collagenous AF is
78 particularly susceptible to AGE modification due to the minimal biological turnover and extended
79 half-life (up to ~120 years) of collagen fibers [16, 17]. Understanding the AF structure-function
80 relationship with non-enzymatic glycation can provide valuable insight into disc mechanical
81 failure mechanisms in diabetic patients, which is pivotal for developing effective therapeutic
82 interventions for tissue failure prevention.

83 Previous in vitro studies examining the effect of non-enzymatic crosslinks on AF uniaxial
84 tensile mechanics have reported increased tissue stiffness and energetic toughness along the
85 evaluated loading directions [18, 19]. Likewise, our recent work, which was the first to investigate
86 AF uniaxial tensile mechanics at physiologically relevant AGE levels, reported that glycation
87 significantly increased AF tensile modulus, failure stress, and energetic toughness in the
88 circumferential-axial direction (**Figure 1A** – ‘Circ-ax specimen’) [20]. Joint-level disc mechanics
89 evaluations from studies that induced in vitro crosslinking or used diabetic rodent models fed by
90 AGEs-rich diets also reported higher joint stability and stiffness [21-25]. Therefore, while clinical
91 observations report more frequent and severe tissue failure with AGE accumulation, in vitro
92 mechanical testing results suggest improved tissue mechanical properties with non-enzymatic
93 crosslinking, leaving the relationship between AGE accumulation and tissue failure unclear.

94 The knowledge of crosslinking structures at the subtissue scale remains limited due to
95 experimental limitations, despite considerable efforts to investigate the functional role of AGEs.
96 Previous work has developed a constitutive relationship to describe AF uniaxial tensile mechanics
97 with non-enzymatic glycation. Still, the relationship was limited to the two-dimensional space and
98 one sample orientation [18]. Finite element models (FEMs) can predict hard-to-measure stress-
99 strain distributions in complex fiber-reinforced tissues. Through combined experimental-FEM
100 study designs, our previous work successfully used FEMs to guide experimental studies and
101 corroborate experimental hypotheses [26, 27]. Additionally, we have developed and validated a
102 multiscale structure-based FEM framework for the AF, which is able to investigate multiscale
103 structure-function relationships in healthy and degenerated AF tissues under various loading and
104 boundary conditions [28-31]. This framework also has the potential to be adapted to describe AF
105 mechanics with non-enzymatic glycation.

106 Thus, the current study aimed to examine the effect of AGEs on anisotropic AF uniaxial
107 tensile mechanics through a combined experimental-computational approach. To achieve this, we
108 evaluated the impact of AGEs on AF uniaxial tensile mechanics on formerly unexamined
109 orientations (circumferential-radial and radial directions). We also adapted our previous multiscale
110 structure-based FEM framework to describe AF mechanics with crosslinking. The validated model
111 was applied to examine subtissue-level stress-strain distributions, aiming to provide mechanistic
112 explanations for premature tissue failure observed with AGE accumulation. Compared to past
113 AGE-oriented AF mechanics studies, the current study was the first to use a combined
114 experimental-FEM approach, which allowed assessment of subtissue-level stress-strain
115 distributions that are difficult to determine directly through bulk tissue experiments. The validated
116 models provided valuable insight into the effect of AGEs at the subtissue scale, including the likely

117 orientation of crosslinking structures and extrafibrillar matrix stress distributions. We
118 hypothesized that the improved bulk AF mechanical properties with non-enzymatic glycation were
119 achieved at the risk of exposing the extrafibrillar matrix to increased damage accumulation through
120 mechanical failure and catabolic remodeling.

121 **2. Materials and methods**

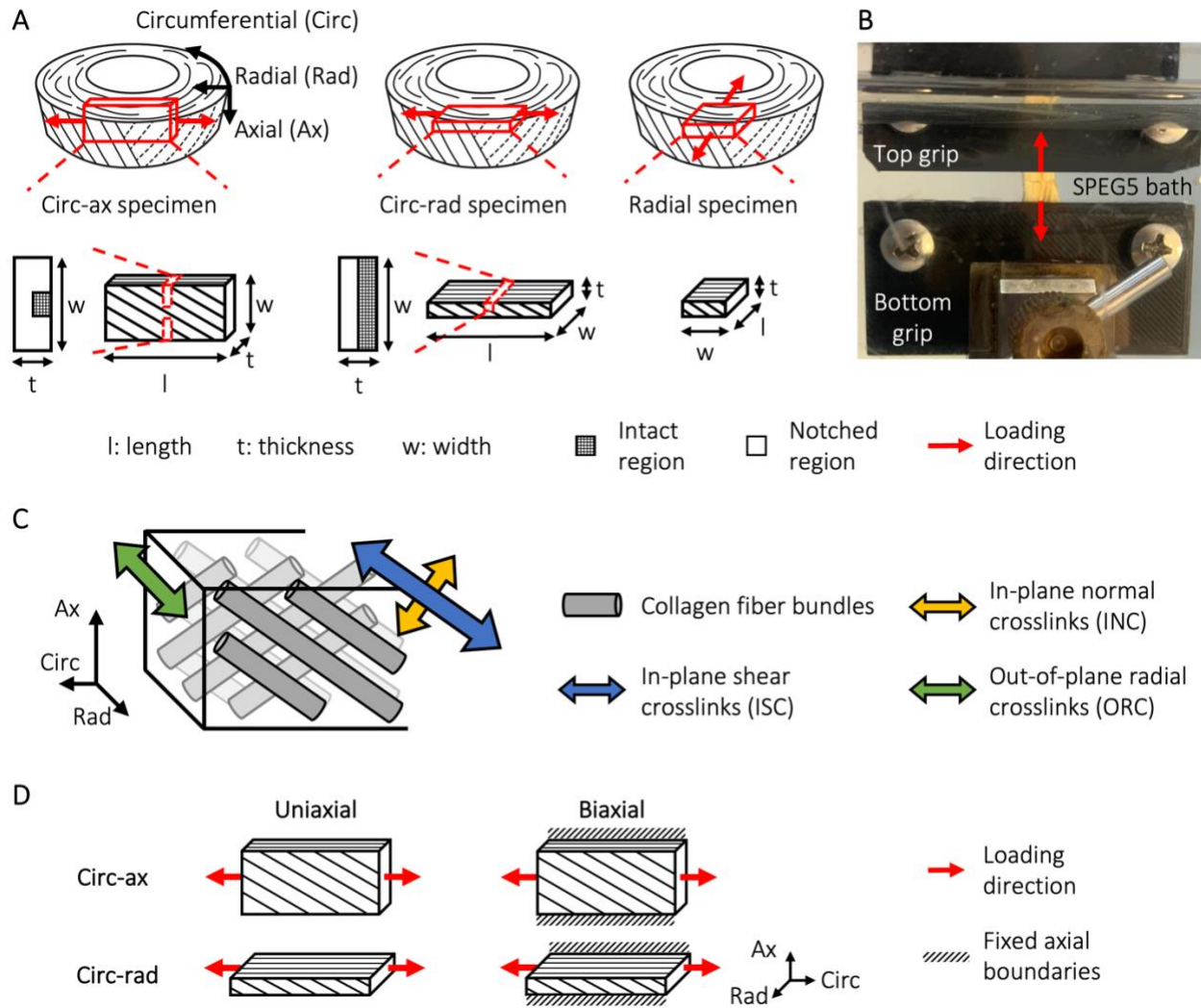
122 **2.1 Experimental testing**

123 **2.1.1 Sample preparation**

124 Bovine discs were used due to their improved accessibility and comparable size,
125 mechanical properties, matrix structures, and biochemical composition to human discs [32-35].
126 Fresh, skeletally mature, healthy bovine caudal spine sections were acquired from a local butcher
127 (age = 18-24 months; n = 10 spines). Musculature around the discs was removed using a scalpel
128 to prepare disc specimens from C2 to C5 (n = 30 discs). AF specimens oriented in the
129 circumferential-radial and radial directions were prepared from the freshly dissected discs (**Figure**
130 **1A** – ‘Circ-rad specimen’ and ‘Radial specimen’). A freezing stage microtome was used to obtain
131 2 mm-thick rectangular specimens. A custom-built cutting tool was used to ensure a specimen
132 width of 5 mm, while sample length depended on the specimen orientation, with an average of 10
133 mm for circumferential-radial and 5 mm for radial samples. Both circumferential-radial and radial
134 specimens contained ~10-15 lamellae. To ensure repeatable midlength failure, a 1 mm thick, full-
135 width notch was created using a custom-made cutting jig in the specimen thickness direction for
136 the circumferential-radial samples [26]. Preliminary testing showed that radial specimens
137 exhibited limited grip failure. Thus, the radial specimens were unnotched. Previous studies
138 reported no significant differences in stiffness or strength between notched and intact fiber-

139 reinforced soft tissue specimens and demonstrated a limited effect of stress concentrations at the
140 notch site [36].

141 Circumferential-radial specimens were prepared with one of the following three soaking
142 protocols to obtain physiologically relevant AGE levels in vitro. Samples in the control group
143 (CTRL) were soaked for 18 hours at 25 °C in a solution containing 5% phosphate-buffer solution
144 and 5% w/v polyethylene glycol (i.e., SPEG5 solution) to minimize excessive tissue swelling [20,
145 27]. Glycated samples were soaked in 0.3 M methylglyoxal at either 25 °C (GLY25) or 50 °C
146 (GLY50) [20]. All soaking solutions were pH-balanced to 7.4, and previous work showed that
147 incubation at 50 °C did not alter bulk AF mechanics or composition [34]. Only CTRL and GLY50
148 groups were prepared for radial specimens, which had collagen fibers oriented perpendicular to
149 the loading direction, resulting in minimal fiber engagement.



150

151 **Figure 1:** (A) Schematics of specimen orientation, loading direction (red arrows), and midlength
 152 notch geometry for the experimental specimens and validation FEMs. (B) Circumferential-radial
 153 sample gripped by the custom-made serrated screw-clamp grips and soaked in an SPEG5 bath
 154 during testing. Red arrows represent the loading direction. Model schematics demonstrating (C)
 155 possible crosslink orientations and (D) simulated uniaxial and biaxial boundary conditions. The
 156 models in (D) were developed to examine multiscale AF mechanics under the uniaxial and biaxial
 157 boundary conditions and were created without a midlength notch.

158 **2.1.2 Mechanical testing**

159 Samples were gripped for mechanical testing using a pair of custom-made serrated screw-
160 clamp grips and were placed in a SPEG5 solution water bath to maintain physiologic tissue
161 hydration throughout testing (up to ~170 min; **Figure 1B**). A monotonic 0.1 N preload was applied
162 to remove slack from the tissue. Scale bar photographs of each specimen were taken to measure
163 the initial sample-specific length (circumferential-radial specimen: 9.64 ± 1.46 mm; radial
164 specimen: 4.94 ± 1.48 mm). Uniaxial tension was applied monotonically along the circumferential
165 direction for the circumferential-radial samples ($n = 15$ per treatment group) and radial direction
166 for the radial samples ($n = 8$ per treatment group) at a quasistatic loading rate (0.1 mm/min,
167 0.017%/sec). Mechanical testing ended when the specimens were separated into two pieces with
168 no load-bearing capability. Rate-dependent differences were assessed for the circumferential-
169 radial specimens at a high loading rate (50 mm/min, 8.33%/sec, $n = 17$ per treatment group).
170 Preliminary testing showed that rate-dependent mechanics variations for these specimens followed
171 a similar trend to that reported for the circumferential-axial samples [20]. Since the objective of
172 the current study was to investigate the effect of AGEs on anisotropic AF uniaxial tensile
173 mechanics, high-rate mechanics data are only presented in **Supplementary figure 1**. Unless
174 otherwise specified, the remainder of this article presents mechanical testing data obtained at the
175 quasistatic loading rate.

176 For each specimen that demonstrated a clean midlength failure, engineering stress-strain
177 response was analyzed to facilitate comparison to the existing literature. Engineering stress was
178 calculated as the measured force divided by the initial cross-sectional area evaluated at specimen
179 midlength. Engineering strain was calculated as the tester crosshead displacement divided by the
180 initial gauge (specimen) length. Bulk tensile modulus was calculated at the linear region to ensure
181 physiologic relevance and facilitate comparison with prior literature. The linear region of the

182 circumferential-radial specimen was identified using a custom linear regression optimization
183 algorithm. The algorithm excluded the toe and yield regions of the stress-strain response and
184 calculated the linear region by determining the maximum range within the stress-strain response
185 in which the change in slope remained within a selected threshold (5%) for strain increments of
186 0.75% (**Figure 2A** – inset). Failure stress and strain were recorded at the maximum force during
187 testing. The ‘failure energy ratio’ was also calculated as the strain energy density up to the point
188 of failure divided by the total strain energy density [20].

189 **2.1.3 Biochemistry**

190 After mechanical testing, a 3 mm biopsy punch was used to extract tissue near the failure
191 sites. Tissue samples were blotted dry using a Kimwipe prior to wet weight measurements. The
192 tissue samples were then lyophilized for 48 hours for dry weight measurements. Water content
193 was calculated as the difference between the wet and dry weight divided by the wet weight.
194 Collagen content was measured using the orthohydroxyproline (OHP) colorimetric assay,
195 assuming a 1:7.5 OHP-to-collagen mass ratio [37]. Total fluorescence, which estimated the AGE
196 content, was assessed using a quinine sulfate standard at excitation/emission wavelengths of 370
197 nm/440 nm and was reported as equivalent nanograms of quinine normalized by tissue dry weight
198 [20]. Biochemistry assessments were conducted on the circumferential-radial specimens.

199 **2.1.4 Statistical methods**

200 A priori power analysis was performed using data reported by Werbner et al. to calculate
201 the necessary sample size to achieve a significance level of 0.05 and a power of 0.95 [20]. Pairwise
202 permutation tests with repeated measures were conducted between treatment groups for all
203 mechanical and biochemical properties, as a few datasets did not pass the Shapiro-Wilk Normality
204 Test. All measurements were reported as mean \pm standard deviation since most datasets (> 80%)

205 followed a normal distribution. Bivariate linear correlations were established between tensile
206 modulus and AGE content and between failure stress and AGE content for the circumferential-
207 radial specimens. Correlation strength was determined based on the correlation coefficient R (weak:
208 $|R| < 0.5$, moderate: $0.50 \leq |R| < 0.70$, strong: $|R| \geq 0.70$). A two-way analysis of covariance
209 (ANCOVA) was performed to compare the regression models for the circumferential-radial
210 specimens in this study to the circumferential-axial regression models reported by Werbner et al.
211 (independent variable: AGE content; fixed factor: specimen orientation) [20]. Significance for the
212 permutation tests and ANCOVA was assumed at $p < 0.05$.

213 **2.2 Finite element modeling**

214 **2.2.1 Model development and validation**

215 For this study, we adapted a previously validated multiscale structure-based FEM
216 framework developed for the AF [28]. For brevity, only essential model development details are
217 provided, but the reader is encouraged to refer to the previous paper for additional information. In
218 short, the AF was modeled as a fiber-reinforced composite, where the extrafibrillar matrix and
219 collagen fiber bundles were described as distinct materials occupying separate volumes, and the
220 fiber bundles were described as full-length cylinders uniformly distributed throughout the lamellae
221 and welded to the surrounding matrix (**Figure 1C**) [28, 38, 39]. The geometries and dimensions
222 of the validation FEMs were developed to represent rectangular experimental specimens oriented
223 in the circumferential-axial, circumferential-radial, and radial directions (**Figure 1A**) [20].
224 Individual AF lamellae were modeled as 0.4 mm thick [40], with collagen fibers orienting at $\pm 35^\circ$
225 to the anatomical transverse plane to represent samples prepared from the middle-outer AF [41].
226 Model geometries also included a midlength notch for the circumferential-axial and
227 circumferential-radial specimens (**Figure 1A**). Circumferential-axial (~950k elements),

228 circumferential-radial (~850k elements), and radial models (~420k elements) contained five,
 229 twelve, and eleven lamellae, respectively, which were consistent with the number of lamellae in
 230 experimental specimens. Model material descriptions and boundary and loading conditions were
 231 defined in FEBio Studio, and the fully defined FEMs were solved by the FEBio solver [42].

232 The triphasic mixture theory was applied to describe tissue hydration [43]. Model fixed
 233 charge density represented tissue proteoglycan content and was set to -100 mmol/L for the matrix
 234 and 0 mmol/L for the fibers [34, 44, 45]. To describe the AF solid phase, the extrafibrillar matrix
 235 was modeled as a Neo-Hookean material [29], where the Young's modulus (0.5 MPa) and
 236 Poisson's ratio (0.3) were determined based on in vitro AF measurements [46, 47]. Collagen fibers
 237 were modeled as a compressible hyperelastic ground matrix substance reinforced by a power-
 238 linear fiber description to describe AF nonlinearity and anisotropy. The ground matrix substance
 239 was modeled using the same Neo-Hookean material described above. For the power-linear fiber
 240 description (**Equation [1]**), β represented the power-law exponent in the toe region, E_{lin}
 241 represented the fiber modulus in the linear region, λ_0 represented the transition stretch between
 242 the toe and linear regions, and B was a function of β , E_{lin} , and λ_0 ($B = \frac{E_{\text{lin}}}{2} (\frac{\lambda_0^2 - 1}{2(\beta - 1)\lambda_0^3} + \frac{1}{\lambda_0})$). Fiber
 243 parameters ($E_{\text{lin}} = 60$ MPa, $\beta = 4$, and $\lambda_0 = 1.09$) were determined based on our previously
 244 validated models and reported AF fiber bundle mechanical testing data [28, 48].

$$245 \quad \psi_n(\lambda_n) = \begin{cases} 0 & \lambda_n < 1 \\ \frac{E_{\text{lin}}}{4\beta(\beta-1)\lambda_0^3} (\lambda_0^2 - 1)^{2-\beta} (\lambda_n - 1)^\beta & 1 \leq \lambda_n \leq \lambda_0 \\ E_{\text{lin}}(\lambda_n - \lambda_0) + B(\lambda_n^2 - \lambda_0^2) + \frac{E_{\text{lin}}}{4\beta(\beta-1)\lambda_0^3} (\lambda_0^2 - 1)^2 & \lambda_n > \lambda_0 \end{cases} \quad [1]$$

246 To account for potential AGE-modifiable fibrous AF crosslinking structures, non-
 247 enzymatic crosslinks were modeled as a combination of three possible components oriented in
 248 mutually perpendicular directions, including (1) in-plane crosslinks parallel to the collagen fibers
 249 (in-plane shear crosslinks), (2) in-plane crosslinks perpendicular to the collagen fibers (in-plane

250 normal crosslinks), and (3) out-of-plane crosslinks oriented in the AF radial direction (out-of-plane
251 radial crosslinks; **Figure 1C**). All crosslink components were modeled as extrafibrillar
252 reinforcements described by the power-linear fiber description (**Equation [1]**). Since no previous
253 evidence has pointed towards variations in crosslink mechanics with orientation, all crosslink
254 components were assumed to share identical material parameters. Nonlinear crosslink material
255 parameters (i.e., β and λ_0) were assigned the same values as the collagen fibers, with exception of
256 the crosslink modulus ($E_{\text{crosslink}}$), which was the calibrated parameter in this study. A higher AGE
257 content was assumed to generate a proportionally greater number of AGEs that could crosslink
258 collagen fibers, resulting in denser AGE compounds per specimen unit volume, and thus a higher
259 apparent crosslink modulus (i.e., $E_{\text{crosslink, GLY50}} = 2 \times E_{\text{crosslink, GLY25}}$).

260 The adapted FEM was validated to ensure its predictive power over AF uniaxial tensile
261 mechanics with non-enzymatic glycation. All validation FEMs were loaded in two steps. To
262 account for specimen hydration, free-swelling was simulated in the SPEG5 external bath [27]. The
263 post-swelling, pre-tension configuration was defined as the reference configuration for mechanics
264 calculations. A uniaxial quasistatic tensile ramp to 40% engineering strain was then applied in the
265 circumferential direction for the circumferential-axial and circumferential-radial models, while a
266 uniaxial quasistatic tensile ramp to 150% radial engineering strain was simulated for the radial
267 model. Displacement on the specimen top and bottom surfaces was constrained to the loading
268 direction throughout the simulated tension. For the circumferential-axial and circumferential-
269 radial models, the tensile modulus was calculated as the slope of the linear region of the
270 engineering stress-strain curve between 25% and 35% engineering strain. The tensile modulus for
271 the radial models was calculated as the slope of the engineering stress-strain response between
272 100% and 150% engineering strain. To ensure an optimal solution for the crosslink modulus

273 calibration, a parametric study was conducted by developing parametric FEMs with varying
274 crosslink modulus ($n = 16$ for circumferential-axial and circumferential-radial models). Model
275 predictions were considered valid if the predicted tensile modulus deviated from the respective
276 reported experimental means by less than 50% of the reported standard deviation.

277 A multivariate linear regression model was used to evaluate the relationship between the
278 increase in AF circumferential tensile modulus and crosslink modulus based on the parametric
279 FEM models. Significance was assumed for $p < 0.05$. The relative contribution of crosslink
280 modulus to the increase in AF circumferential tensile modulus was calculated using the relaimpo
281 package in R and reported as a percentage [49].

282 **2.2.2 Effect of non-enzymatic glycation on multiscale AF mechanics**

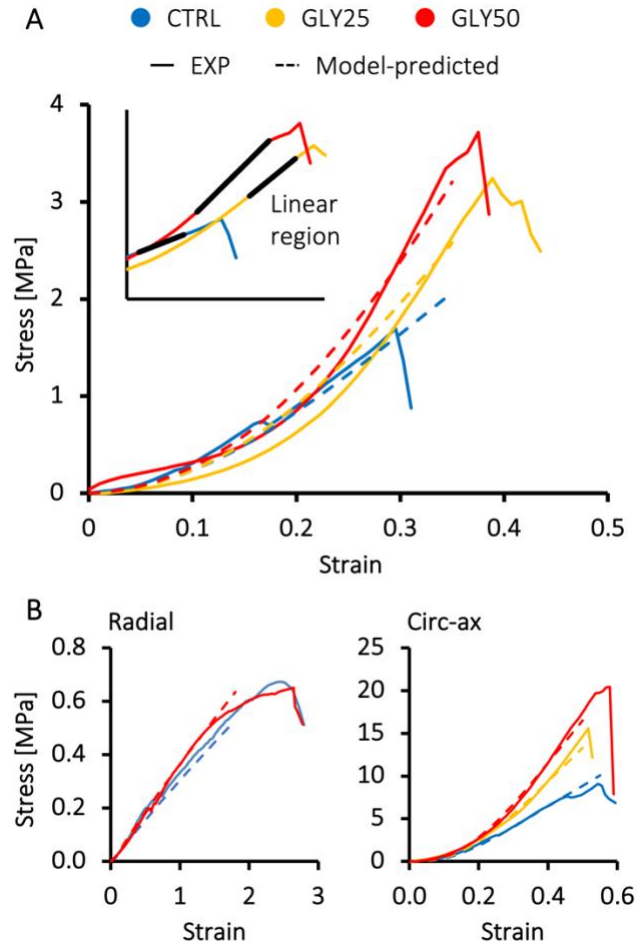
283 Following model validation, another set of circumferential-axial and circumferential-radial
284 models was developed to investigate the effect of non-enzymatic glycation on multiscale AF
285 mechanics. While model dimensions still mimicked the samples for mechanical testing, the
286 midlength notch geometry was excluded (**Figure 1D**). Models were developed to represent the
287 CTRL and GLY50 samples loaded under uniaxial and biaxial boundary conditions. For the
288 uniaxial models, the boundary and loading conditions were identical to the validation FEMs. For
289 the biaxial models, the axial boundaries were fixed throughout the simulated quasistatic tension,
290 which was applied in the circumferential direction to 40% engineering strain (**Figure 1D**). The
291 post-swelling, pre-tension configuration was defined as the reference configuration. The apparent
292 bulk tensile modulus was calculated as the slope of the linear region of the engineering stress-
293 strain curve between 25% and 35% engineering strain. The average stress in the extrafibrillar
294 matrix and fibers were evaluated throughout the simulated tension. The percentage of failed tissue
295 elements was evaluated at 0.5 MPa circumferential stress due to physiologic relevance [40], which

296 was calculated as the applied circumferential load divided by the respective specimen cross-
297 sectional area. To ensure the repeatability of our model predictions, the percentage of tissue failure
298 was also evaluated using a strain-based assumption at 15% circumferential engineering strain,
299 which corresponds to the largest internal AF strain observed in vitro in intact discs under
300 physiologically relevant loadings [50, 51]. Failure of individual tissue elements was assessed using
301 a stress-based criterion. Bulk AF radial failure stress was considered representative of matrix
302 failure stress due to the minimum fiber engagement in that orientation. The failure stress threshold
303 for the fibers was determined based on data in the literature [52]. The failure threshold was set at
304 75% of the respective mean failure stress to better represent tissue failure initiation following
305 yielding [53].

306 **3. Results**

307 **3.1 Experimental testing**

308 Circumferential-radial specimens demonstrated a nonlinear bulk stress-strain response,
309 while radial samples showed a pseudo-linear bulk stress-strain response prior to bulk tissue failure
310 (**Figure 2** – colored solid lines). A clear linear region was observed for all circumferential-radial
311 specimens (**Figure 2A** – inset). A maximum stress that corresponded to bulk tissue failure was
312 observed for all specimens. Mechanical testing data was only analyzed for samples that
313 demonstrated a clean midlength failure (circumferential-radial: 73% of total specimens, n = 11 per
314 treatment group; radial: 88% of total specimens, n = 7 per treatment group).

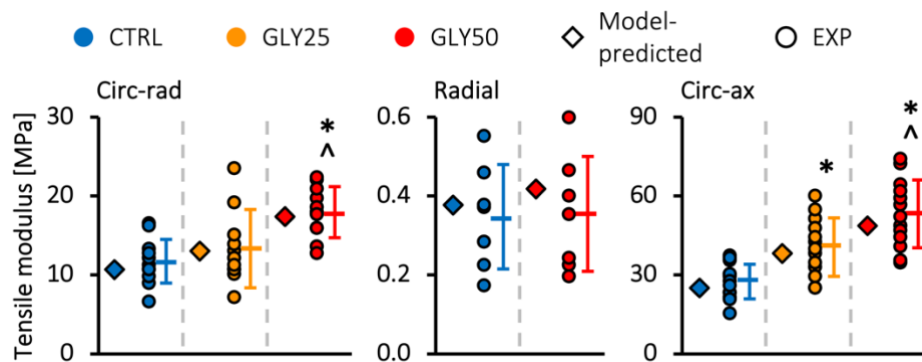


315

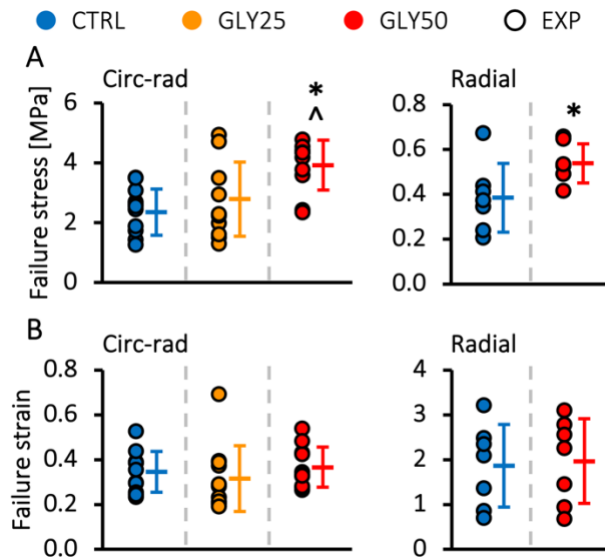
316 **Figure 2:** Representative experimental (EXP) and model-predicted engineering stress-strain
 317 curves at each glycation level for (A) circumferential-radial and (B) radial and circumferential-
 318 axial specimens. Data reported for circumferential-axial samples were adapted from Werbner et
 319 al. for model validation [20]. Inset in (A) demonstrates the linear regions calculated by the custom
 320 linear regression optimization algorithm using bolded black line segments.

321 For circumferential-radial specimens, the GLY50 treatment increased the tensile modulus
 322 by 53% compared to the CTRL group (CTRL: 11.73 ± 2.76 MPa, GLY50: 17.96 ± 3.24 MPa, $p <$
 323 0.001) and by 35% compared to the GLY25 group (GLY25: 13.33 ± 4.95 MPa, $p = 0.013$; **Figure**
 324 **3 – Circ-rad**). The GLY50 treatment also increased the failure stress by 57% compared to the
 325 CTRL group (CTRL: 2.35 ± 0.77 MPa, GLY50: 3.69 ± 0.83 MPa, $p < 0.001$) and by 32%

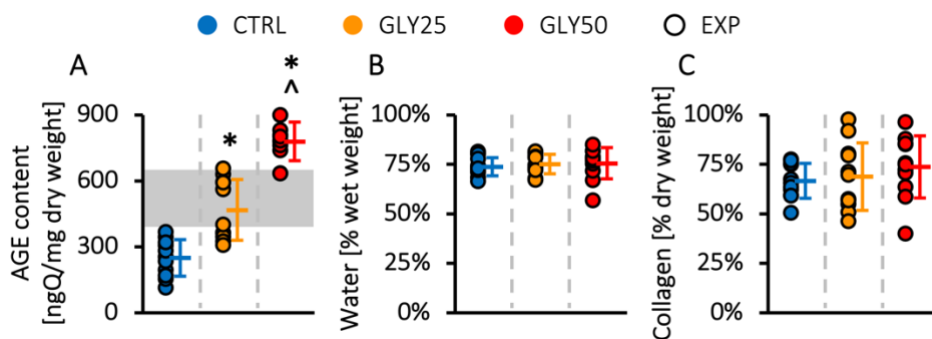
326 compared to the GLY25 group (GLY25: 2.79 ± 1.24 MPa, $p = 0.012$; **Figure 4A** – Circ-rad).
 327 However, the tensile modulus and failure stress of the GLY25 samples were not different from the
 328 CTRL specimens ($p > 0.35$). For radial specimens, the GLY50 treatment increased the failure
 329 stress by 40% compared to the CTRL group (CTRL: 0.39 ± 0.15 MPa, GLY50: 0.54 ± 0.09 MPa,
 330 $p = 0.043$; **Figure 4A** – Radial). However, the tensile modulus was not affected by the glycation
 331 treatment ($p > 0.90$; **Figure 3** – Radial). Non-enzymatic glycation did not affect tissue failure strain
 332 in both tested orientations and all treatment groups ($p > 0.35$; **Figure 4B**). Additionally, a trend in
 333 failure energy ratio was not observed with non-enzymatic glycation.



334 **Figure 3:** Experimental tensile modulus (circles) compared to model predictions (diamonds) at
 335 each glycation level for all three specimen orientations. Data reported for circumferential-axial
 336 samples are reproduced from Werbner et al. for model validation [20]. * represents $p < 0.001$ vs.
 337 CTRL; ^ represents $p < 0.05$ vs. GLY25.



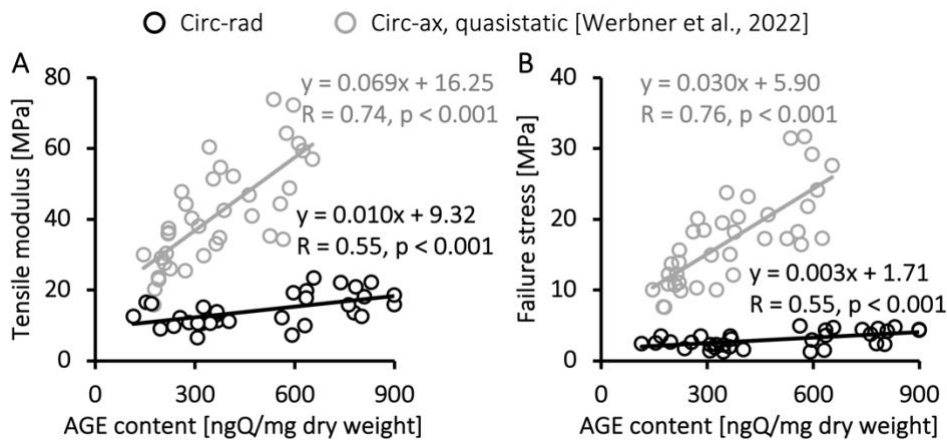
339
 340 **Figure 4:** (A) Failure stress and (B) failure strain at each glycation level for both specimen
 341 orientations. * represents $p < 0.05$ vs. CTRL; ^ represents $p < 0.05$ vs. GLY25.



342
 343 **Figure 5:** (A) AGE, (B) water, and (C) collagen content at each glycation level. The gray region
 344 in (A) represents the range of AGE content measured in human discs [20]. * represents $p < 0.001$
 345 vs. CTRL; ^ represents $p < 0.001$ vs. GLY25.

346 AGE content normalized by tissue dry weight increased by 87% with the GLY25 treatment
 347 (CTRL: 250 ± 84 ngQ/mg dry weight; GLY25: 468 ± 138 ngQ/mg dry weight, $p < 0.001$) and by
 348 ~210% with the GLY50 treatment (GLY50: 779 ± 87 ngQ/mg dry weight, $p < 0.001$). The AGE
 349 content of the GLY50 group was ~65% higher than the GLY25 group ($p < 0.001$; **Figure 5A**).
 350 Water and collagen content were not affected by the glycation treatment (**Figures 5B** and **5C**).

351 In the circumferential-radial direction, there was a moderate positive correlation between
 352 AGE content and tensile modulus ($R = 0.55$, $p < 0.001$; **Figure 6A** – black trendline); a moderate
 353 positive correlation was also observed between AGE content and failure stress ($R = 0.55$, $p <$
 354 0.0001 ; **Figure 6B** – black trendline). Specimen orientation had a significant effect on the
 355 relationship between AGE content and tensile modulus and between AGE content and failure
 356 stress (ANCOVA $p < 0.001$), with the tensile properties of circumferential-axial specimens being
 357 more sensitive to AGE accumulation (**Figure 6** – gray vs. black trendlines).



358 **Figure 6:** Bivariate linear correlation between (A) tensile modulus and (B) failure stress and AGE
 359 content for circumferential-radial samples (black circles). Quasistatic circumferential-axial data
 360 reported by Werbner et al. were shown for comparison (gray circles) [20]. Regression models
 361 obtained for the two specimen orientations were significantly different (ANCOVA $p < 0.001$).

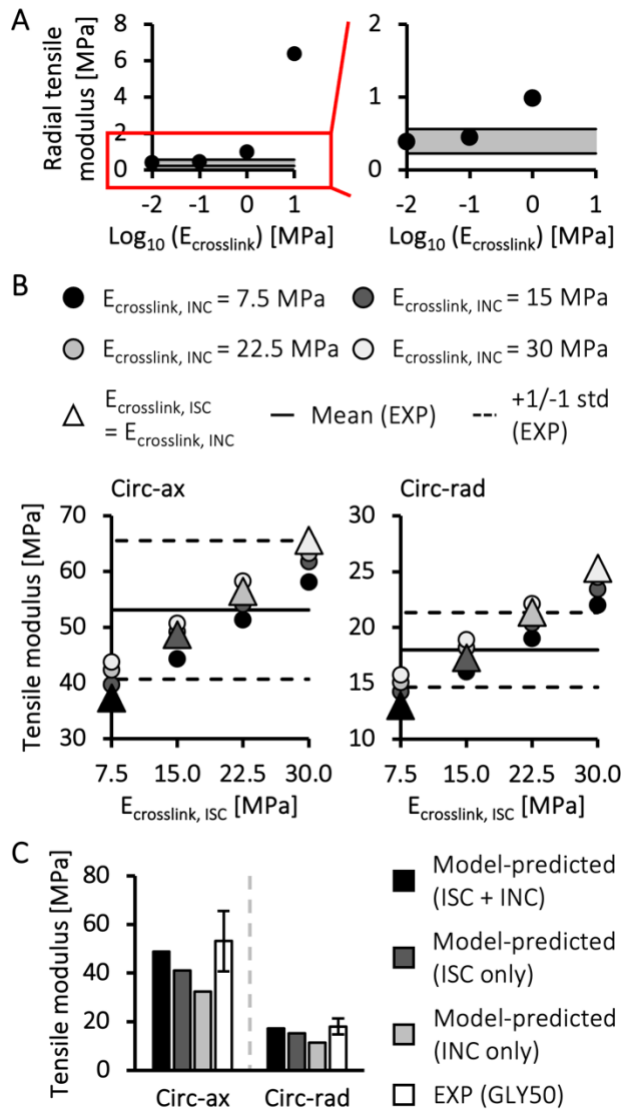
363 3.2 Finite element modeling

364 3.2.1 Model validation

365 With all three possible crosslink components (i.e., in-plane shear crosslinks, in-plane
 366 normal crosslinks, and out-of-plane radial crosslinks, **Figure 1C**), model predictions showed that
 367 a crosslink modulus lower than 0.1 MPa was required to predict an AF radial tensile modulus
 368 within the range of existing experimental data (**Figure 7A**). Meanwhile, FEMs with a crosslink

369 modulus of 10 MPa predicted an AF radial tensile modulus of 6.38 MPa, more than 10× higher
370 than the largest AF radial tensile modulus reported (**Figure 7A**). However, a crosslink modulus
371 greater than 7.5 MPa was required to generate model predictions within around one standard
372 deviation of the mean circumferential tensile modulus values (**Figure 7B**). Therefore, out-of-plane
373 radial crosslinks were not included in the model (**Figure 1C**). Model predictions also showed that
374 FEMs with only in-plane shear crosslinks or in-plane normal crosslinks greatly underestimated AF
375 circumferential tensile modulus for the GLY50 group (**Figure 7C**). Thus, both in-plane shear
376 crosslinks and in-plane normal crosslinks were necessary and therefore included in the model.

377 Adapted FEMs accurately and robustly predicted experimental measurements when the
378 crosslink modulus was 12.5% of collagen fibers (i.e., 7.5 MPa) in the GLY25 model and 25% of
379 collagen fibers (i.e., 15 MPa) in the GLY50 model, which was further confirmed by the parametric
380 FEM predictions (**Figure 7B**). Model predictions matched well with experimental stress-strain
381 responses in all specimen orientations and all treatment groups (**Figure 2** – colored dashed vs.
382 solid lines). Model-predicted bulk AF tensile modulus values were within 0.4× standard deviation
383 from the experimental means in all specimen orientations and all treatment groups (**Figure 3**).
384 Thus, the adapted FEMs were considered valid for describing and investigating AF tensile
385 mechanics with non-enzymatic glycation.



386

387 **Figure 7:** (A) Model-predicted AF radial tensile modulus with varying crosslink modulus ($E_{\text{crosslink}}$
 388 = 0.01 MPa, 0.1 MPa, 1 MPa, and 10 MPa). Predicted values were compared to the AF radial
 389 tensile modulus range reported in the literature, highlighted by the gray region [40, 54-56]. (B)
 390 Model-predicted tensile modulus for circumferential-axial and circumferential-radial specimens
 391 with varying crosslink modulus. Horizontal solid and dashed lines represent the range of
 392 experimental data (mean \pm standard deviation, std). (C) Model-predicted circumferential tensile
 393 modulus for GLY50 specimens with varying crosslinking structures vs. experimental data.

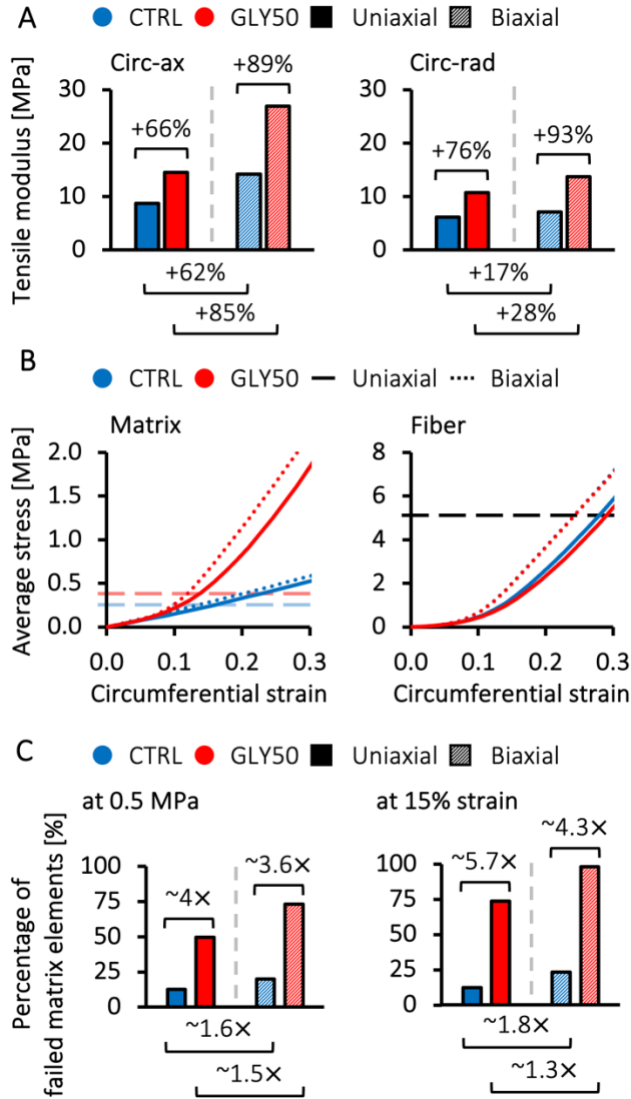
394 Multivariate linear regression models were able to explain more than 99.5% of the variance
395 in parametric FEMs. Terms associated with the out-of-plane radial crosslinks were excluded from
396 the models. The increase in AF circumferential tensile modulus increased linearly with in-plane
397 shear and in-plane normal crosslink modulus ($p < 0.001$ for both crosslink types and specimen
398 orientations) but did not depend on their interactions (**Equations [2]** and **[3]**). The relative
399 contribution analysis suggested that the increase in AF circumferential tensile modulus was more
400 sensitive to the in-plane shear than the in-plane normal crosslink modulus. Particularly, the in-
401 plane shear crosslink modulus contributed to ~90% of the increase in circumferential tensile
402 modulus in both orientations, while the in-plane normal crosslink modulus only contributed ~10%.

$$403 \quad \Delta E_{\text{Circ-ax}} = 4.62 + 0.91 \times E_{\text{crosslink,ISC}} + 0.27 \times E_{\text{crosslink,INC}} + \varepsilon \quad [2]$$

$$404 \quad \Delta E_{\text{Circ-rad}} = 0.21 + 0.41 \times E_{\text{crosslink,ISC}} + 0.13 \times E_{\text{crosslink,INC}} + \varepsilon \quad [3]$$

405 **3.2.2 Effect of non-enzymatic glycation on multiscale AF mechanics**

406 For circumferential-axial models, the biaxial boundary condition increased the apparent
407 tensile modulus by 62-85% (**Figure 8A** – Circ-ax, diagonal vs. solid bars). Glycation had a
408 comparable effect, increasing the apparent tensile modulus by 66-89% (**Figure 8A** – Circ-ax, red
409 vs. blue bars). For circumferential-radial models, the biaxial boundary condition had a less
410 pronounced effect, only increasing the apparent tensile modulus by 17-28% (**Figure 8A** – Circ-
411 rad, diagonal vs. solid bars); however, glycation increased the apparent tensile modulus by more
412 than 75% (**Figure 8A** – Circ-rad, red vs. blue bars).



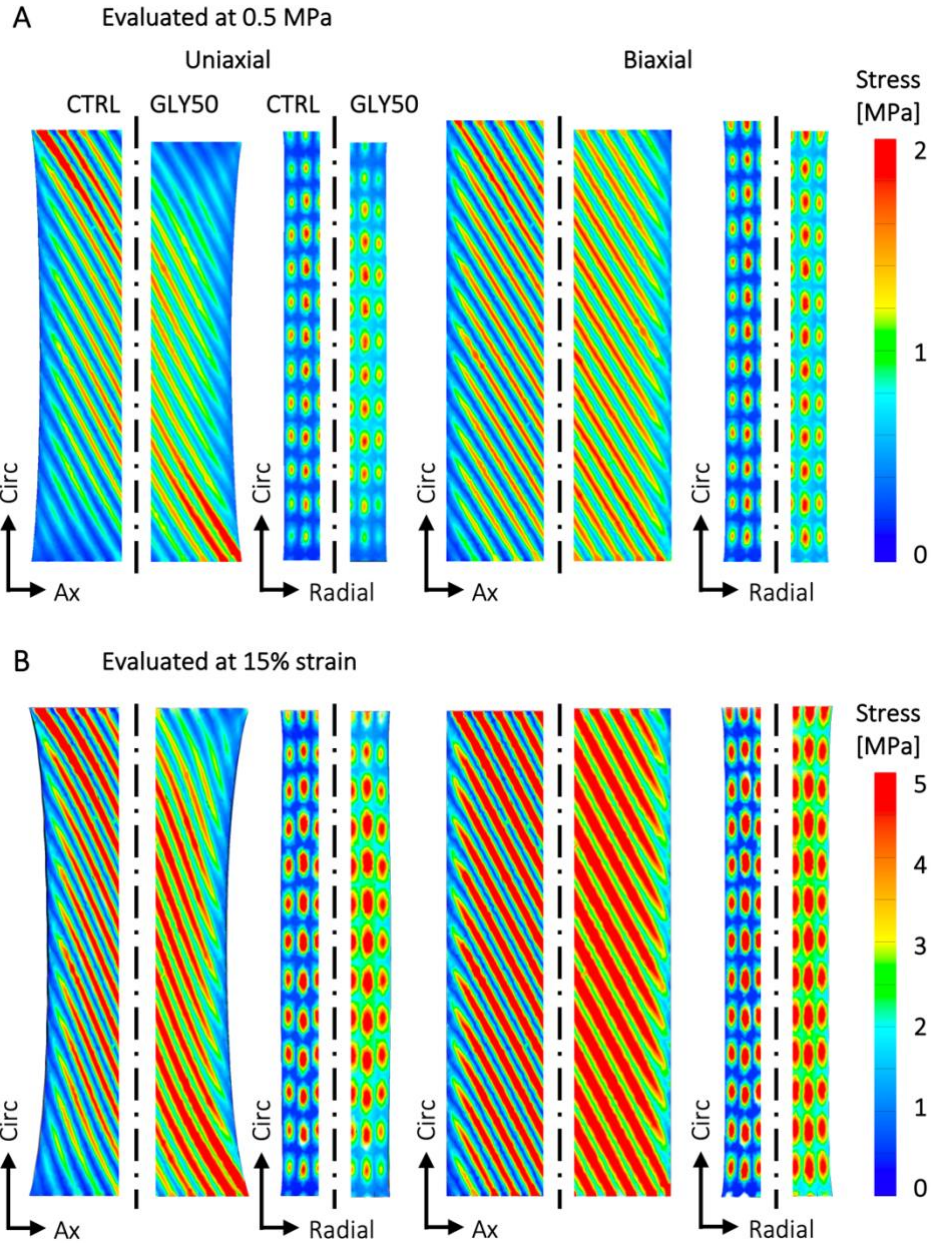
413

414 **Figure 8:** Model-predicted (A) circumferential tensile apparent modulus, (B) average matrix and
 415 fiber stress. The light blue and red horizontal dashed lines represent the stress thresholds for failed
 416 matrix elements in CTRL and GLY50 models, respectively. The black dashed line represents the
 417 failure stress threshold for fibers [52]. (C) Percentage of failed matrix elements evaluated at 0.5
 418 MPa circumferential stress and 15% engineering strain.

419 Model predictions indicated that glycation had a greater impact on subtissue-level
 420 mechanics than altered boundary conditions, especially in the extracellular matrix (**Figures 8B,**
 421 **8C,** and **9**). Under 0.5 MPa, the average matrix stress in the uniaxial circumferential-axial CTRL

422 model was 0.25 MPa and increased by ~60% to 0.40 MPa with glycation (**Figure 8B** – Matrix,
423 solid blue vs. red lines; **Figure 9A**). Simulating a biaxial boundary condition only increased the
424 average matrix stress by less than 5% (**Figure 8B** – Matrix, blue solid vs. dotted lines; **Figure 9A**).
425 Based on the failure criterion calculated using the measured AF radial failure stress (CTRL: 0.39
426 MPa \times 75% = 0.29 MPa; GLY50: 0.54 MPa \times 75% = 0.40 MPa; **Figure 4A**), glycation led to a
427 ~4 \times increase in the percentage of failed matrix elements from 13% to 50% under uniaxial tension
428 at 0.5 MPa (**Figure 8C** – red vs. blue solid bars), while biaxial loading resulted in a ~1.5 \times increase
429 in the percentage of failed matrix elements (**Figure 8C** – diagonal vs. solid blue bars). In the
430 circumferential-axial biaxial models, glycation increased the average matrix stress by ~90% from
431 0.30 to 0.56 MPa (**Figure 8B** – Matrix, dotted blue vs. red lines; **Figure 9A**), resulting in over 70%
432 of the matrix elements exceeding the failure threshold (**Figure 8C** – at 0.5 MPa, diagonal red bar).
433 A similar trend was observed when evaluating failure using a strain-controlled assumption at 15%
434 engineering strain (**Figure 8C** – at 15% strain; **Figure 9B**).

435 Contrary to the changes in matrix mechanics, the average fiber stress was largely
436 unaffected by glycation (**Figure 8B** – Fiber, red vs. blue lines; **Figure 9**). At 0.5 MPa
437 circumferential stress or 15% engineering strain, increasing the boundary constraints with the
438 biaxial boundary increased the average fiber stress by 20-70%, but the average fiber stress
439 remained well below the failure threshold (**Figure 8B** – Fiber, solid vs. dotted lines). A similar
440 trend was observed for models oriented in the circumferential-radial direction.



441

442 **Figure 9:** (A) Representative frontal and side midplane stress distributions at 0.5 MPa
 443 circumferential stress for CTRL and GLY50 models. Stress in the extrafibrillar matrix increased
 444 with glycation, changing from dark blue shading in the CTRL to green in the GLY50 models. Red
 445 shadings represent higher stresses in the fibers (vs. the matrix). (B) Representative stress
 446 distributions at 15% applied circumferential engineering strain showed a similar trend.

447 **Discussion**

448 The study investigated the relationship between physiologic levels of advanced glycation
449 end-products and anisotropic AF uniaxial tensile mechanics using a combined experimental-
450 computational approach. In vitro glycation increased AF tensile modulus and failure stress in the
451 circumferential-radial direction (**Figures 3 and 4A**), agreeing with previous observations reported
452 for circumferential-axial samples [19, 20]. However, for circumferential-radial specimens,
453 changes in tensile mechanics with AGE accumulation were not as pronounced (**Figure 6**) [20].
454 Specifically, the in vitro glycation treatments led to comparable increases in AGE content in both
455 specimen orientations [20]. However, the GLY50 treatment increased the AF tensile modulus and
456 failure stress by ~100% for the circumferential-axial specimens but only by ~50% for the
457 circumferential-radial specimens. While the GLY25 treatment led to statistically significant
458 increases in circumferential-axial tensile modulus and failure stress, it did not affect the
459 circumferential-radial specimens (**Figures 3 and 4A**). Additionally, multivariate linear regression
460 predicted that the modulus of in-plane shear crosslinks, which are parallel to the collagen fibers,
461 contributed to approximately 90% of the increase in tensile modulus. The primary distinction
462 between circumferential-axial and circumferential-radial specimens lies in the loading direction
463 relative to the orientation and length of the collagen fibers. In particular, collagen fibers in the
464 circumferential-radial specimen extended across the 2 mm thickness, while fibers in the
465 circumferential-axial sample traversed the entire 5 mm width, resulting in a larger effective fiber
466 length and fiber engagement [29, 57]. Taken together, these findings indicated that non-enzymatic
467 crosslinks had the greatest impact along the collagen fiber direction, with this effect increasing
468 with intact fiber length and fiber engagement.

469 Non-enzymatic glycation had a smaller effect on AF radial mechanics, where fiber
470 engagement was minimal during loading. Specifically, the GLY50 treatment did not affect the

471 tissue modulus and only increased the failure stress by 40% (**Figures 3 and 4A**). FEM predictions
472 also suggested a negligible effect from the AGEs in the radial direction (**Figure 1C**), as including
473 out-of-plane radial crosslinks led to unrealistically high radial tensile modulus (**Figure 7A**). While
474 defining a smaller modulus for the radial crosslinks (i.e., 0.01-0.1 MPa) compared to the in-plane
475 crosslinks produced realistic AF radial tensile modulus predictions (**Figure 7A**), we did not find
476 previous evidence supporting stiffness variations between AGEs compounds derived from the
477 same collagen type. Previous two-dimensional constitutive models developed to describe AF
478 mechanics with glycation also suggested that in-plane crosslinks were sufficient [18]. Furthermore,
479 elastin proteins, the main constituents of interlamellar elastic fibers oriented in the AF radial
480 direction, only accounted for 2% of tissue dry weight, indicating a low likelihood of elastin-derived
481 AGEs compounds (i.e., out-of-plane radial crosslinks) [58-60]. A multiphoton autofluorescence
482 study further complemented these findings by demonstrating that collagens were more responsive
483 to AGE formation than interlamellar elastic fibers [61]. Thus, our results agree with and add to the
484 existing literature regarding the crosslinking structure by showing that interlamellar radial
485 crosslinks are unlikely to form in the AF.

486 Studies that evaluate mechanical properties of human disc soft tissues are known to report
487 large variations. While reported mechanics variations between studies can be attributed to
488 differences in specimen geometry [29], variations within studies might, in part, be due to
489 differences in tissue composition with degeneration and disease. For example, coefficients of
490 variation (i.e., the ratio of the standard deviation to the mean) for the tensile modulus of healthy
491 anterior outer circumferential-axial AF specimens, whose structure and morphology are expected
492 to be relatively uniform, still range from 0.56 to 0.82 [53, 55, 56, 62]. This study evaluated a
493 parametric group of crosslink modulus values corresponding to different AGE levels to determine

494 the effect of AGE accumulation on bulk tissue mechanics. The parametric models predicted a
495 range of modulus values that spanned the experimental variations reported in both specimen
496 orientations (**Figure 7B**). This finding suggested that large variations observed in human disc
497 mechanical properties may be in part due to variations in AGE content, which are often not
498 accounted for during tissue degeneration level evaluations (e.g., Thompson scale) [63].

499 AGE accumulation occurs naturally with aging and has been linked to various soft tissue
500 diseases besides disc degenerative disorders, such as osteoarthritis and tendinopathy [15, 64, 65].
501 Studies using diabetic rodent models also reported significantly reduced tendon modulus and
502 failure stress [66, 67]. However, conflicting results have been reported in vitro. In addition to the
503 increased AF energetic toughness reported in the current and previous AF studies [18-20], non-
504 enzymatic glycation in vitro has been found to increase tissue stiffness and failure stress in other
505 soft fiber-reinforced soft tissues, such as tendons, cartilages, and corneas [68-72]. In vitro
506 crosslinking also enhanced tissue resistance to collagen degradation and mechanical wear [73].
507 Researchers have partially attributed this discrepancy to the uncoupling of exogenous AGE
508 accumulation from natural cellular and tissue remodeling in response to a high AGE extracellular
509 environment, which is known to induce cellular inflammatory responses [24, 74-77]. Alternatively,
510 tendon studies reported that AGE treatment significantly reduced tissue viscoelastic properties (i.e.,
511 energy dissipation capabilities) [69, 70], suggesting that diabetic crosslinking might induce
512 premature tissue failure by compromising tissue performance under fatigue loading. Additionally,
513 tendon studies have shown that non-enzymatic glycation may result in tissue stiffening due to
514 diminished interfibrillar sliding [69, 70, 72, 78]. Similar mechanisms may be at play in the AF,
515 despite the differences in tissue composition and fiber orientation; however, interfibrillar sliding
516 was beyond the scope of this study.

517 In this study, subtissue-level FEM predictions provided another probable explanation for
518 this discrepancy between in vivo and in vitro tissue failure behavior with AGE accumulation.
519 Under a physiologically relevant strain (i.e., $\leq 15\%$ strain) or stress range (i.e., ~ 0.5 MPa),
520 glycation greatly increased the stress in the extrafibrillar matrix, predisposing a larger portion of
521 the tissue to a greater risk of mechanical failure (**Figures 8B and C**). The current study evaluated
522 matrix failure under both stress- and strain-controlled methods, as both approaches have been used
523 frequently and interchangeably in experimental and computational studies [79]. As such, the
524 improved bulk AF tensile mechanical properties with AGE accumulation were achieved at the risk
525 of exposing the extrafibrillar matrix to increased mechanical damage accumulation. Additionally,
526 previous cellular biology studies showed that higher stresses applied to AF cells caused
527 inflammatory responses, which may also trigger premature tissue failure through catabolic
528 remodeling [80-82]. Lastly, future experimental work is needed to confirm that findings from this
529 study are translatable to human disc tissues.

530 The biaxial boundary condition was simulated in the current study due to its physiologic
531 relevance and difficulties in conducting repeatable soft tissue biaxial tensile testing in vitro. Model
532 predictions highlighted that glycation had a greater effect on AF bulk and subtissue-level
533 mechanics than the evaluated biaxial boundary condition (i.e., an axial-fixed condition), especially
534 on the stresses in the extrafibrillar matrix (**Figure 8B**). However, the more constrained biaxial
535 boundary amplified the effect of glycation, disposing nearly all the matrix elements in the GLY50
536 biaxial model to failure under large physiologic deformations (**Figure 8C**). This amplifying effect
537 may be more pronounced in vivo, as the heavily glycated tissues would be more restricted by the
538 surrounding structures (e.g., the nucleus and endplates), further increasing the risk of tissue failure.

539 One limitation of the current study was that tissue proteoglycan content was not
540 characterized. However, previous in vitro studies consistently reported that AGE treatment did not
541 affect proteoglycan content, regardless of the crosslinking agent used [83-85]. Tissue water content,
542 a benchmark for proteoglycan content, also remained at the fresh tissue level for all treatment
543 groups (**Figure 5B**), suggesting that proteoglycan was unaffected by the methylglyoxal-based
544 treatment. While AGE content in discs from diabetic patients has not been characterized, the AGE
545 content induced in GLY25 specimens aligned well with the range measured from human cadaveric
546 disc tissues, while CTRL and GLY50 specimens covered the lower and higher end of that range
547 (**Figure 5A**) [20], making our specimens justifiable candidate tissue models to examine the
548 differences between healthy and diabetic tissues. Another limitation was that the current study did
549 not characterize the elastin-derived AGE content, which could have a considerable effect on AF
550 mechanics, especially with degeneration [59]. Computationally, crosslinks were described as
551 extrafibrillar reinforcements. Future models may need to explicitly describe crosslinks to
552 differentiate failure originating from the extrafibrillar matrix from the crosslinks themselves, as
553 well as to understand the relative contribution of fiber stiffening and reduced interfibrillar sliding
554 to bulk tissue strengthening with glycation, which remains a debate in the field [69, 70, 72, 78].

555 **4. Conclusions**

556 The current study evaluated the effects of AGEs on anisotropic AF uniaxial tensile
557 mechanics using a combined experimental-computational approach. Experimentally, AF uniaxial
558 tensile mechanical properties were reported in circumferential-radial and radial directions at three
559 physiologically relevant AGE levels. Computationally, multiscale structure-based FEMs were
560 developed and validated to describe crosslinks within the extrafibrillar matrix. The validated
561 models were used to examine the effect of glycation on multiscale AF mechanics under uniaxial

562 and biaxial boundary conditions. Mechanical testing results showed that in vitro glycation did not
563 lead to compromised AF mechanical properties under monotonic quasistatic uniaxial tension in
564 both tested orientations, agreeing with previous literature. The proposed FEM framework
565 accurately predicted AF bulk tensile mechanics with glycation and provided insight into the
566 relationship between AGE accumulation and more frequent and severe tissue failure observed with
567 diabetes. Specifically, glycation exposed the extrafibrillar matrix to greater stresses under
568 physiologically relevant deformations, which may lead to increased tissue failure through greater
569 accumulated mechanical damage or catabolic tissue remodeling. Our findings also suggested
570 probable crosslinking structures at the subtissue level, indicating that AGEs had a more
571 pronounced effect along the fiber direction, while interlamellar radial crosslinks were less likely
572 to form in the AF. In conclusion, the improved bulk mechanical properties of fiber-reinforced
573 biological tissues with AGE accumulation may be achieved at the risk of exposing the extrafibrillar
574 matrix to larger stresses under physiologic deformations, leading to premature tissue failure. The
575 presented combined approach provides a powerful tool for examining multiscale AF structure-
576 function relationships with disease progression, which is crucial for developing effective
577 preventive measures and therapeutic interventions for low back pain.

578 **5. Acknowledgements**

579 Funding: This work was supported by National Science Foundation [CAREER #1751212 – GDO;
580 GRFP #DGE 2146752 – ESA].

581 This material is based upon work supported by the National Science Foundation Graduate
582 Research Fellowship Program under Grant No. DGE 2146752. Any opinions, findings, and
583 conclusions or recommendations expressed in this material are those of the author(s) and do not
584 necessarily reflect the views of the National Science Foundation.

585 **References**

- 586 [1] Hoy, D., March, L., Brooks, P., Blyth, F., Woolf, A., Bain, C., Williams, G., Smith, E., Vos,
587 T., Barendregt, J. and Murray, C., 2014. The global burden of low back pain: estimates from the
588 Global Burden of Disease 2010 study. *Annals of the rheumatic diseases*, 73(6), pp.968-974.
589
- 590 [2] Bloom, D.E., Boersch-Supan, A., McGee, P. and Seike, A., 2011. Population aging: facts,
591 challenges, and responses. *Benefits and compensation International*, 41(1), p.22.
592
- 593 [3] Popkin, B.M., 2015. Nutrition transition and the global diabetes epidemic. *Current diabetes*
594 *reports*, 15, pp.1-8.
595
- 596 [4] Zhou, B., Lu, Y., Hajifathalian, K., Bentham, J., Di Cesare, M., Danaei, G., Bixby, H.,
597 Cowan, M.J., Ali, M.K., Taddei, C. and Lo, W.C., 2016. Worldwide trends in diabetes since
598 1980: a pooled analysis of 751 population-based studies with 4· 4 million participants. *The*
599 *lancet*, 387(10027), pp.1513-1530.
600
- 601 [5] Jakoi, A.M., Pannu, G., D'oro, A., Buser, Z., Pham, M.H., Patel, N.N., Hsieh, P.C., Liu, J.C.,
602 Acosta, F.L., Hah, R. and Wang, J.C., 2017. The clinical correlations between diabetes, cigarette
603 smoking and obesity on intervertebral degenerative disc disease of the lumbar spine. *Asian spine*
604 *journal*, 11(3), p.337.
605
- 606 [6] Liu, X., Pan, F., Ba, Z., Wang, S. and Wu, D., 2018. The potential effect of type 2 diabetes
607 mellitus on lumbar disc degeneration: a retrospective single-center study. *Journal of Orthopaedic*
608 *Surgery and Research*, 13(1), pp.1-5.
609
- 610 [7] Steelman, T., Lewandowski, L., Helgeson, M., Wilson, K., Olsen, C. and Gwinn, D., 2018.
611 Population-based risk factors for the development of degenerative disk disease. *Clinical spine*
612 *surgery*, 31(8), pp.E409-E412.
613
- 614 [8] Russo, F., Ambrosio, L., Ngo, K., Vadalà, G., Denaro, V., Fan, Y., Sowa, G., Kang, J.D. and
615 Vo, N., 2019. The role of type I diabetes in intervertebral disc degeneration. *Spine*, 44(17),
616 p.1177.
617
- 618 [9] Jhawar, B.S., Fuchs, C.S., Colditz, G.A. and Stampfer, M.J., 2006. Cardiovascular risk
619 factors for physician-diagnosed lumbar disc herniation. *The spine journal*, 6(6), pp.684-691.
620
- 621 [10] Raj, P.P., 2008. Intervertebral disc: anatomy -physiology -pathophysiology -treatment. *Pain*
622 *Practice*, 8(1), pp.18-44.
623
- 624 [11] Adams, M.A. and Roughley, P.J., 2006. What is intervertebral disc degeneration, and what
625 causes it?. *Spine*, 31(18), pp.2151-2161.
626
- 627 [12] Vergroesen, P.P., Kingma, I., Emanuel, K.S., Hoogendoorn, R.J., Welting, T.J., van Royen,
628 B.J., van Dieën, J.H. and Smit, T.H., 2015. Mechanics and biology in intervertebral disc
629 degeneration: a vicious circle. *Osteoarthritis and cartilage*, 23(7), pp.1057-1070.

630 [13] Vlassara, H. and Palace, M.R., 2002. Diabetes and advanced glycation endproducts. *Journal*
631 *of internal medicine*, 251(2), pp.87-101.
632

633 [14] Ahmed, N. and Thornalley, P.J., 2007. Advanced glycation endproducts: what is their
634 relevance to diabetic complications?. *Diabetes, Obesity and Metabolism*, 9(3), pp.233-245.
635

636 [15] Suzuki, A., Yabu, A. and Nakamura, H., 2022. Advanced glycation end products in
637 musculoskeletal system and disorders. *Methods*, 203, pp.179-186.
638

639 [16] Verzijl, N., DeGroot, J., Thorpe, S.R., Bank, R.A., Shaw, J.N., Lyons, T.J., Bijlsma, J.W.,
640 Lafeber, F.P., Baynes, J.W. and TeKoppele, J.M., 2000. Effect of collagen turnover on the
641 accumulation of advanced glycation end products. *Journal of Biological Chemistry*, 275(50),
642 pp.39027-39031.
643

644 [17] Snedeker, J.G. and Gautieri, A., 2014. The role of collagen crosslinks in ageing and
645 diabetes-the good, the bad, and the ugly. *Muscles, ligaments and tendons journal*, 4(3), p.303.
646

647 [18] Wagner, D.R., Reiser, K.M. and Lotz, J.C., 2006. Glycation increases human annulus
648 fibrosus stiffness in both experimental measurements and theoretical predictions. *Journal of*
649 *biomechanics*, 39(6), pp.1021-1029.
650

651 [19] Chuang, S.Y., Odonon, R.M. and Hedman, T.P., 2007. Effects of exogenous crosslinking on
652 in vitro tensile and compressive moduli of lumbar intervertebral discs. *Clinical Biomechanics*,
653 22(1), pp.14-20.
654

655 [20] Werbner, B., Lee, M., Lee, A., Yang, L., Habib, M., Fields, A.J. and O'Connell, G.D., 2022.
656 Non-enzymatic glycation of annulus fibrosus alters tissue-level failure mechanics in tension.
657 *Journal of the Mechanical Behavior of Biomedical Materials*, 126, p.104992.
658

659 [21] Hedman, T.P., Saito, H., Vo, C. and Chuang, S.Y., 2006. Exogenous cross-linking increases
660 the stability of spinal motion segments. *Spine*, 31(15), pp.E480-E485.
661

662 [22] Barbir, A., Michalek, A.J., Abbott, R.D. and Iatridis, J.C., 2010. Effects of enzymatic
663 digestion on compressive properties of rat intervertebral discs. *Journal of biomechanics*, 43(6),
664 pp.1067-1073.
665

666 [23] Kirking, B.C., Toungate, J.K. and Hedman, T.P., 2013. The dose response relationship
667 between intervertebral disc flexion-extension neutral zone metrics and injected genipin
668 concentration. *Journal of applied biomaterials & functional materials*, 11(2), pp.73-79.
669

670 [24] Fields, A.J., Berg-Johansen, B., Metz, L.N., Miller, S., La, B., Liebenberg, E.C., Coughlin,
671 D.G., Graham, J.L., Stanhope, K.L., Havel, P.J. and Lotz, J.C., 2015. Alterations in intervertebral
672 disc composition, matrix homeostasis and biomechanical behavior in the UCD-T2DM rat model
673 of type 2 diabetes. *Journal of orthopaedic research*, 33(5), pp.738-746.
674

675 [25] Krishnamoorthy, D., Hoy, R.C., Natelson, D.M., Torre, O.M., Laudier, D.M., Iatridis, J.C.
676 and Illien-Jünger, S., 2018. Dietary advanced glycation end-product consumption leads to
677 mechanical stiffening of murine intervertebral discs. *Disease Models & Mechanisms*, 11(12),
678 p.dmm036012.
679

680 [26] Werbner, B., Zhou, M. and O'Connell, G., 2017. A novel method for repeatable failure
681 testing of annulus fibrosus. *Journal of biomechanical engineering*, 139(11).
682

683 [27] Werbner, B., Zhou, M., McMIndes, N., Lee, A., Lee, M. and O'Connell, G.D., 2022. Saline-
684 polyethylene glycol blends preserve in vitro annulus fibrosus hydration and mechanics: An
685 experimental and finite-element analysis. *Journal of the Mechanical Behavior of Biomedical*
686 *Materials*, 125, p.104951.
687

688 [28] Zhou, M., Bezci, S.E. and O'Connell, G.D., 2020. Multiscale composite model of fiber-
689 reinforced tissues with direct representation of sub-tissue properties. *Biomechanics and*
690 *Modeling in Mechanobiology*, 19, pp.745-759.
691

692 [29] Zhou, M., Werbner, B. and O'Connell, G.D., 2021. Fiber engagement accounts for
693 geometry-dependent annulus fibrosus mechanics: A multiscale, Structure-Based Finite Element
694 Study. *Journal of the mechanical behavior of biomedical materials*, 115, p.104292.
695

696 [30] Zhou, M., Lim, S. and O'Connell, G.D., 2021. A robust multiscale and multiphasic
697 structure-based modeling framework for the intervertebral disc. *Frontiers in Bioengineering and*
698 *Biotechnology*, 9, p.685799.
699

700 [31] Zhou, M., Huff, R.D., Abubakr, Y. and O'Connell, G.D., 2022. Torque-and muscle-driven
701 flexion induce disparate risks of in vitro herniation: A multiscale and multiphasic structure-based
702 finite element study. *Journal of biomechanical engineering*, 144(6), p.061005.
703

704 [32] Demers, C.N., Antoniou, J. and Mwale, F., 2004. Value and limitations of using the bovine
705 tail as a model for the human lumbar spine. *Spine*, 29(24), pp.2793-2799.
706

707 [33] O'Connell, G.D., Vresilovic, E.J. and Elliott, D.M., 2007. Comparison of animals used in
708 disc research to human lumbar disc geometry. *Spine*, 32(3), pp.328-333.
709

710 [34] Bezci, S.E., Werbner, B., Zhou, M., Malollari, K.G., Dorlhiac, G., Carraro, C., Streets, A.
711 and O'Connell, G.D., 2019. Radial variation in biochemical composition of the bovine caudal
712 intervertebral disc. *Jor Spine*, 2(3), p.e1065.
713

714 [35] Yu, J., Tirlapur, U., Fairbank, J., Handford, P., Roberts, S., Winlove, C.P., Cui, Z. and
715 Urban, J., 2007. Microfibrils, elastin fibres and collagen fibres in the human intervertebral disc
716 and bovine tail disc. *Journal of anatomy*, 210(4), pp.460-471.
717

718 [36] Taylor, D., O'Mara, N., Ryan, E., Takaza, M. and Simms, C., 2012. The fracture toughness
719 of soft tissues. *Journal of the mechanical behavior of biomedical materials*, 6, pp.139-147.
720

721 [37] Hollander, A.P., Heathfield, T.F., Webber, C., Iwata, Y., Bourne, R., Rorabeck, C. and
722 Poole, A.R., 1994. Increased damage to type II collagen in osteoarthritic articular cartilage
723 detected by a new immunoassay. *The Journal of clinical investigation*, 93(4), pp.1722-1732.
724

725 [38] Marchand, F. and Ahmed, A.M., 1990. Investigation of the laminate structure of lumbar
726 disc annulus fibrosus. *Spine*, 15(5), pp.402-410.
727

728 [39] Schollum, M.L., Robertson, P.A. and Broom, N.D., 2010. How age influences unravelling
729 morphology of annular lamellae—a study of interfibre cohesivity in the lumbar disc. *Journal of*
730 *anatomy*, 216(3), pp.310-319.
731

732 [40] Holzapfel, G.A., Schulze-Bauer, C.A., Feigl, G. and Regitnig, P., 2005. Single lamellar
733 mechanics of the human lumbar annulus fibrosus. *Biomechanics and modeling in*
734 *mechanobiology*, 3, pp.125-140.
735

736 [41] Matcher, S.J., Winlove, C.P. and Gangnus, S.V., 2004. The collagen structure of bovine
737 intervertebral disc studied using polarization-sensitive optical coherence tomography. *Physics in*
738 *Medicine & Biology*, 49(7), p.1295.
739

740 [42] Maas, S.A., Ellis, B.J., Ateshian, G.A. and Weiss, J.A., 2012. FEBio: finite elements for
741 biomechanics.
742

743 [43] Lai, W.M., Hou, J.S. and Mow, V.C., 1991. A triphasic theory for the swelling and
744 deformation behaviors of articular cartilage.
745

746 [44] Urban, J.P.G. and Maroudas, A., 1979. The measurement of fixed charged density in the
747 intervertebral disc. *Biochimica et Biophysica Acta (BBA)-General Subjects*, 586(1), pp.166-178.
748

749 [45] Antoniou, J., Steffen, T., Nelson, F., Winterbottom, N., Hollander, A.P., Poole, R.A., Aebi,
750 M. and Alini, M., 1996. The human lumbar intervertebral disc: evidence for changes in the
751 biosynthesis and denaturation of the extracellular matrix with growth, maturation, ageing, and
752 degeneration. *The Journal of clinical investigation*, 98(4), pp.996-1003.
753

754 [46] Cao, L., Guilak, F. and Setton, L.A., 2009. Pericellular matrix mechanics in the annulus
755 fibrosus predicted by a three-dimensional finite element model and in situ morphology. *Cellular*
756 *and molecular bioengineering*, 2, pp.306-319.
757

758 [47] Périé, D., Korda, D. and Iatridis, J.C., 2005. Confined compression experiments on bovine
759 nucleus pulposus and annulus fibrosus: sensitivity of the experiment in the determination of
760 compressive modulus and hydraulic permeability. *Journal of biomechanics*, 38(11), pp.2164-
761 2171.
762

763 [48] Pham, D.T., Shapter, J.G. and Costi, J.J., 2018. Tensile behaviour of individual fibre
764 bundles in the human lumbar annulus fibrosus. *Journal of biomechanics*, 67, pp.24-31.
765

766 [49] Grömping, U., 2007. Relative importance for linear regression in R: the package relaimpo.
767 Journal of statistical software, 17, pp.1-27.
768

769 [50] Heuer, F., Schmidt, H. and Wilke, H.J., 2008. The relation between intervertebral disc
770 bulging and annular fiber associated strains for simple and complex loading. Journal of
771 biomechanics, 41(5), pp.1086-1094.
772

773 [51] O'Connell, G.D., Vresilovic, E.J. and Elliott, D.M., 2011. Human intervertebral disc internal
774 strain in compression: the effect of disc region, loading position, and degeneration. Journal of
775 orthopaedic research, 29(4), pp.547-555.
776

777 [52] Skaggs, D.L., Weidenbaum, M., Iatridis, J.C., Ratcliffe, A. and Mow, V.C., 1994. Regional
778 variation in tensile properties and biochemical composition of the human lumbar annulus fibrosus.
779 Spine, 19(12), pp.1310-1319.
780

781 [53] Acaroglu, E.R., Iatridis, J.C., Setton, L.A., Foster, R.J., Mow, V.C. and Weidenbaum, M.,
782 1995. Degeneration and aging affect the tensile behavior of human lumbar annulus fibrosus.
783 Spine, 20(24), pp.2690-2701.
784

785 [54] Fujita, Y., Duncan, N.A. and Lotz, J.C., 1997. Radial tensile properties of the lumbar
786 annulus fibrosus are site and degeneration dependent. Journal of orthopaedic research, 15(6),
787 pp.814-819.
788

789 [55] Elliott, D.M. and Setton, L.A., 2001. Anisotropic and inhomogeneous tensile behavior of
790 the human annulus fibrosus: experimental measurement and material model predictions. J.
791 Biomech. Eng., 123(3), pp.256-263.
792

793 [56] O'Connell, G.D., Guerin, H.L. and Elliott, D.M., 2009. Theoretical and uniaxial
794 experimental evaluation of human annulus fibrosus degeneration.
795

796 [57] Adams, M.A. and Green, T.P., 1993. Tensile properties of the annulus fibrosus: I. The
797 contribution of fibre-matrix interactions to tensile stiffness and strength. European Spine Journal,
798 2, pp.203-208.
799

800 [58] Cloyd, J.M. and Elliott, D.M., 2007. Elastin content correlates with human disc
801 degeneration in the annulus fibrosus and nucleus pulposus. Spine, 32(17), pp.1826-1831.
802

803 [59] Smith, L.J. and Fazzalari, N.L., 2009. The elastic fibre network of the human lumbar annulus
804 fibrosus: architecture, mechanical function and potential role in the progression of intervertebral
805 disc degeneration. European Spine Journal, 18, pp.439-448.
806

807 [60] Cyril, D., Giugni, A., Bangar, S.S., Mirzaeipoueinak, M., Shrivastav, D., Sharabi, M.,
808 Tipper, J.L. and Tavakoli, J., 2022. Elastic fibers in the intervertebral disc: From form to
809 function and toward regeneration. International Journal of Molecular Sciences, 23(16), p.8931.
810

811 [61] Tseng, J.Y., Ghazaryan, A.A., Lo, W., Chen, Y.F., Hovhannisyan, V., Chen, S.J., Tan, H.Y.
812 and Dong, C.Y., 2011. Multiphoton spectral microscopy for imaging and quantification of tissue
813 glycation. *Biomedical optics express*, 2(2), pp.218-230.
814

815 [62] Ebara, S., Iatridis, J.C., Setton, L.A., Foster, R.J., Mow, V.C. and Weidenbaum, M., 1996.
816 Tensile properties of nondegenerate human lumbar anulus fibrosus. *Spine*, 21(4), pp.452-461.
817

818 [63] Thompson, J.P., Pearce, R.H., Schechter, M.T., Adams, M.E., Tsang, I.K. and Bishop, P.B.,
819 1990. Preliminary evaluation of a scheme for grading the gross morphology of the human
820 intervertebral disc. *Spine*, 15(5), pp.411-415.
821

822 [64] Handl, M.I.L.A.N., Filova, E., Kubala, M., Lánský, Z., Koláčná, L., Vorlíček, J., Trč, T.,
823 Pach, M. and Amler, E., 2007. Fluorescent advanced glycation end products in the detection of
824 factual stages of cartilage degeneration. *Physiological research*, 56(2).
825

826 [65] Lui, P.P.Y., 2017. Tendinopathy in diabetes mellitus patients—epidemiology, pathogenesis,
827 and management. *Scandinavian journal of medicine & science in sports*, 27(8), pp.776-787.
828

829 [66] de Oliveira, R.R., de Lira, K.D.S., de Castro Silveira, P.V., Coutinho, M.P.G., Medeiros,
830 M.N., Teixeira, M.F.H.B.I. and de Moraes, S.R.A., 2011. Mechanical properties of achilles
831 tendon in rats induced to experimental diabetes. *Annals of biomedical engineering*, 39, pp.1528-
832 1534.
833

834 [67] Fox, A.J., Bedi, A., Deng, X.H., Ying, L., Harris, P.E., Warren, R.F. and Rodeo, S.A., 2011.
835 Diabetes mellitus alters the mechanical properties of the native tendon in an experimental rat
836 model. *Journal of Orthopaedic Research*, 29(6), pp.880-885.
837

838 [68] Avila, M.Y. and Navia, J.L., 2010. Effect of genipin collagen crosslinking on porcine
839 corneas. *Journal of Cataract & Refractive Surgery*, 36(4), pp.659-664.
840

841 [69] Li, Y., Fessel, G., Georgiadis, M. and Snedeker, J.G., 2013. Advanced glycation end-
842 products diminish tendon collagen fiber sliding. *Matrix Biology*, 32(3-4), pp.169-177.
843

844 [70] Gautieri, A., Passini, F.S., Silván, U., Guizar-Sicairos, M., Carimati, G., Volpi, P., Moretti,
845 M., Schoenhuber, H., Redaelli, A., Berli, M. and Snedeker, J.G., 2017. Advanced glycation end-
846 products: Mechanics of aged collagen from molecule to tissue. *Matrix Biology*, 59, pp.95-108.
847

848 [71] Reddy, G.K., Stehno-Bittel, L. and Enwemeka, C.S., 2002. Glycation-induced matrix
849 stability in the rabbit achilles tendon. *Archives of biochemistry and biophysics*, 399(2), pp.174-
850 180.
851

852 [72] Svensson, R.B., Smith, S.T., Moyer, P.J. and Magnusson, S.P., 2018. Effects of maturation
853 and advanced glycation on tensile mechanics of collagen fibrils from rat tail and Achilles
854 tendons. *Acta biomaterialia*, 70, pp.270-280.
855

856 [73] McGann, M.E., Bonitsky, C.M., Jackson, M.L., Ovaert, T.C., Trippel, S.B. and Wagner,
857 D.R., 2015. Genipin crosslinking of cartilage enhances resistance to biochemical degradation and
858 mechanical wear. *Journal of Orthopaedic Research®*, 33(11), pp.1571-1579.
859

860 [74] Yoshida, T., Park, J.S., Yokosuka, K., Jimbo, K., Yamada, K., Sato, K., Takeuchi, M.,
861 Yamagishi, S.I. and Nagata, K., 2009. Up-regulation in receptor for advanced glycation end-
862 products in inflammatory circumstances in bovine coccygeal intervertebral disc specimens in
863 vitro. *Spine*, 34(15), pp.1544-1548.
864

865 [75] Hu, Y., Shao, Z., Cai, X., Liu, Y., Shen, M., Yao, Y., Yuan, T., Wang, W., Ding, F. and
866 Xiong, L., 2019. Mitochondrial pathway is involved in advanced glycation end products-induced
867 apoptosis of rabbit annulus fibrosus cells. *Spine*, 44(10), p.E585.
868

869 [76] Hoy, R.C., D'Erminio, D.N., Krishnamoorthy, D., Natelson, D.M., Laudier, D.M., Illien-Jü
870 nger, S. and Iatridis, J.C., 2020. Advanced glycation end products cause RAGE-dependent
871 annulus fibrosus collagen disruption and loss identified using in situ second harmonic generation
872 imaging in mice intervertebral disk in vivo and in organ culture models. *JOR spine*, 3(4),
873 p.e1126.
874

875 [77] Illien-Junger, S., Grosjean, F., Laudier, D.M., Vlassara, H., Striker, G.E. and Iatridis, J.C.,
876 2013. Combined anti-inflammatory and anti-AGE drug treatments have a protective effect on
877 intervertebral discs in mice with diabetes. *PLoS One*, 8(5), p.e64302.
878

879 [78] Fessel, G., Li, Y., Diederich, V., Guizar-Sicairos, M., Schneider, P., Sell, D.R., Monnier,
880 V.M. and Snedeker, J.G., 2014. Advanced glycation end-products reduce collagen molecular
881 sliding to affect collagen fibril damage mechanisms but not stiffness. *PloS one*, 9(11),
882 p.e110948.
883

884 [79] Costi, J.J., Ledet, E.H. and O'Connell, G.D., 2021. Spine biomechanical testing
885 methodologies: the controversy of consensus vs scientific evidence. *JOR spine*, 4(1), p.e1138.
886

887 [80] Rannou, F., Richette, P., Benallaoua, M., François, M., Genries, V., Korwin-Zmijowska, C.,
888 Revel, M., Corvol, M. and Poiraudou, S., 2003. Cyclic tensile stretch modulates proteoglycan
889 production by intervertebral disc annulus fibrosus cells through production of nitrite oxide.
890 *Journal of cellular biochemistry*, 90(1), pp.148-157.
891

892 [81] Gawri, R., Rosenzweig, D.H., Krock, E., Ouellet, J.A., Stone, L.S., Quinn, T.M. and
893 Haglund, L., 2014. High mechanical strain of primary intervertebral disc cells promotes secretion
894 of inflammatory factors associated with disc degeneration and pain. *Arthritis research & therapy*,
895 16(1), pp.1-14.
896

897 [82] Dombrowski, M.E., Olsen, A.S., Vaudreuil, N., Couch, B.K., Dong, Q., Tucci, M., Lee,
898 J.Y., Vo, N.V. and Sowa, G., 2020. Rabbit annulus fibrosus cells express neuropeptide Y, which
899 is influenced by mechanical and inflammatory stress. *Neurospine*, 17(1), p.69.
900

- 901 [83] Yerramalli, C.S., Chou, A.I., Miller, G.J., Nicoll, S.B., Chin, K.R. and Elliott, D.M., 2007.
902 The effect of nucleus pulposus crosslinking and glycosaminoglycan degradation on disc
903 mechanical function. *Biomechanics and modeling in mechanobiology*, 6, pp.13-20.
904
- 905 [84] Jazini, E., Sharan, A.D., Morse, L.J., Dyke, J.P., Aronowitz, E.A., Chen, L.K. and Tang,
906 S.Y., 2012. Alterations in magnetic resonance imaging T2 relaxation times of the ovine
907 intervertebral disc due to non-enzymatic glycation. *Spine*, 37(4), p.E209.
908
- 909 [85] Liu, J.W., Abraham, A.C. and Tang, S.Y., 2015. The high-throughput phenotyping of the
910 viscoelastic behavior of whole mouse intervertebral discs using a novel method of dynamic
911 mechanical testing. *Journal of biomechanics*, 48(10), pp.2189-2194.